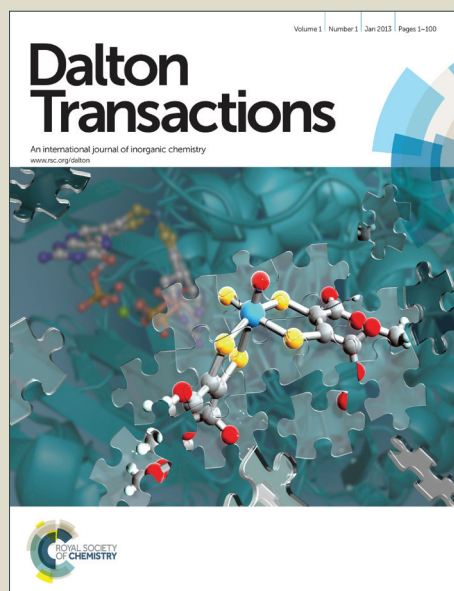


Dalton Transactions

Accepted Manuscript

This article can be cited before page numbers have been issued, to do this please use: G. Gómez, M. C. Bernini, E. Brusau, G. Narda, D. R. Vega, A. Kaczmarek, R. Van Deun and M. Nazzarro, *Dalton Trans.*,



This is an *Accepted Manuscript*, which has been through the Royal Society of Chemistry peer review process and has been accepted for publication.

Accepted Manuscripts are published online shortly after acceptance, before technical editing, formatting and proof reading. Using this free service, authors can make their results available to the community, in citable form, before we publish the edited article. We will replace this *Accepted Manuscript* with the edited and formatted *Advance Article* as soon as it is available.

You can find more information about *Accepted Manuscripts* in the [Information for Authors](#).

Please note that technical editing may introduce minor changes to the text and/or graphics, which may alter content. The journal's standard [Terms & Conditions](#) and the [Ethical guidelines](#) still apply. In no event shall the Royal Society of Chemistry be held responsible for any errors or omissions in this *Accepted Manuscript* or any consequences arising from the use of any information it contains.

ARTICLE

Cite this: DOI: 10.1039/x0xx00000x

Received 00th January 2012,
Accepted 00th January 2012

DOI: 10.1039/x0xx00000x

www.rsc.org/

Layered exfoliable crystalline materials based on Sm-, Eu- and Eu/Gd- 2-phenylsuccinate frameworks. Crystal structure, topology and luminescence properties

G. E. Gomez^a, M. C. Bernini^a, E. V. Brusau^a, G. E. Narda^{*a}, D. Vega^b, A. M. Kaczmarek^c, R. Van Deun^c and M. Nazzarro^d.

ABSTRACT Three new layered metal-organic frameworks (MOFs) based on 2-phenylsuccinic acid (H₂psa) and lanthanide ions, with formula [Ln₂(C₁₀H₈O₄)₃(H₂O)] (Ln= Eu, Sm and Eu-Gd) have been synthesized under solvothermal conditions and fully characterized by single-crystal X-ray diffraction, thermal and vibrational analysis. The compounds are isostructural featuring 2D frameworks that consist of infinite zig-zag chains composed by [LnO₈] and [LnO₈(H₂O)] edge-sharing polyhedra linked by psa ligands leading to layers further connected by weak π - π interactions in an edge orientation. Moreover, a topological study was carried out to obtain the simplified net for better comparison with structurally related compounds. The **Eu-psa** crystals were exfoliated into nanolayers after miniaturization by addition of sodium acetate as capping agent in the reaction medium. Scanning electron microscopy was applied to characterize the miniaturized samples whereas the exfoliated hybrid nanosheets were studied by atomic force microscopy. The photoluminescence (PL) properties of the bulk compounds as well as the miniaturized and exfoliated materials were investigated and compared with other related ones. An exhaustive study of the Eu(III)-based MOFs was performed on the basis of the obtained PL parameters (excitation and emission spectra, k_r , k_{nr} , intrinsic quantum yields and lifetimes) to explore the underlying structure-property relationships.

1. Introduction

In recent years, the design and synthesis of lanthanide-containing coordination polymers have developed into a significant area of research on the basis of their intriguing frameworks and potential applications in several fields. Particularly, their luminescence properties that enable these materials to be employed as sensors¹, optical fiber lasers and amplifiers², molecular thermometers³ and electroluminescent materials⁴ have received increasing attention.⁵

MOFs offer a unique platform and methodology for the development of luminescent lanthanide materials not only because of some well described synthesis methods and resulting porosities, but also for certain degree of structural tenability.⁶ The structures of the resulting MOFs can be tailored through variations of the linkers, templates and growth conditions.

Regarding the selection of the linkers, the variety of available aliphatic and aromatic dicarboxylate ligands offers the possibility to develop diverse architectures with specific structure-properties relationships.⁷ For example, 1D or 2D MOFs exhibiting properties such as luminescence, magnetism or mechanic-elastic properties are suitable to be studied by “top-down” approaches as precursors for creating continuous thin films^{8,9} or to be integrated with other matrices (e.g., polymers) to form robust composite materials.¹⁰ Furthermore, MOFs having only weak inter-layer interactions in their structures can be exfoliated in nanosheets by simple methods such as ultrasonication, opening the possibility to obtain functional thin films by controlled deposition.¹¹ Succinic acid (H₂suc) is a symmetrical and flexible dicarboxylic acid that has been widely combined with transition metal (TM) and rare earth (REE) ions giving raise to numerous

MOFs with 1D, 2D and 3D covalent connectivity.¹² In addition, the use of 2,2- or 2,3- methyl- substituted succinate as linker (2,2-dms, and 2,3-dms, respectively) evidences a tendency to develop 2D covalent frameworks in those cases in which the bulky groups are both located on the same carbon atom.¹³ Interestingly, several of these MOFs based on TM ions and 2,2-dms were successfully exfoliated in nanosheets by the mentioned “top-down” methodologies, augmenting their technological applications through the development of magnetic thin films.¹¹

The asymmetric 2-phenylsuccinic acid (H₂psa), with a more bulky substituent, seems to be a good candidate to develop low dimensional frameworks, since the disposal of the phenyl groups involves a significant steric requirement that may lead to weak inter-chain or inter-layer interactions. Even though this ligand has been poorly explored as building block, the tendency mentioned above has been demonstrated in a few examples involving TM ions: five 1D and 2D MOFs based on Cu(II) and different auxiliary molecules¹⁴, one 1D Zn(II) MOF and one 2D Ni(II) MOF.¹⁵ As far as we know, the interaction between REE ions and H₂psa for the construction of functional MOFs has not been studied.

Regarding the inorganic component, Eu(III) and Tb(III) are the preferred among the whole lanthanide ions for optical devices due to their intense, long-lived, and line-like emission in the visible region. Encouraged by this fact, we have recently reported luminescent 3D MOFs constructed by 2,3-dms ligand where those containing Eu(III) and Tb(III) ions exhibited strong red and green emissions, respectively.^{13c}

However, it is a well-known fact that Ln(III) centers cannot efficiently absorb light due to forbidden 4*f*-4*f* transitions (the extinction coefficient for such trivalent cations is about 1-10 M⁻¹ cm⁻¹).¹⁶ One strategy to sensitize Ln-MOF luminescence is to incorporate chromophores either as linkers or guest molecules that act as antennas for light absorption.¹⁷ The luminescence intensity can also be enhanced by energy transfer from one lanthanide to another lanthanide ion and several heterolanthanide MOFs based mainly on Eu(III) or Tb(III) have been reported.^{18,19,20} TM alo4ng with lanthanide ions have also been probed in the construction of luminescent heterometal-organic frameworks (HMOFs) because the coexistence of heterometallic ions not only contributes to obtaining fascinating structures but can in some cases also tune the energy levels of the MOFs.^{21,22}

Finally, nanoscale processability is another attractive characteristic offered by the MOF approach that enable the application of luminescent MOFs, particularly in the fields of biology, drug delivery, and biomedical imaging in which the nanoscale materials are essential for their internalization into cells.^{23,24} Furthermore, nano-MOFs (NMOFs) display higher surface areas than their macroscopic counterparts and unique size-dependent properties.²⁵

With all these design concepts in mind, we have continued our studies on REE-MOFs selecting the system containing the 2-phenylsuccinate ligand (psa) and Sm(III) or Eu(III) ions, as pure inorganic matrices. Furthermore, focusing on the second

and most interesting ion, two strategies were carried out to optimize the obtaining of MOFs with improved photoluminescence (PL) properties. On the one hand, the synthesis conditions were modified to reduce the particle size and a post-synthetic treatment was applied later to exfoliate the MOF particles to achieve nanoscale dimensions. On the other hand, the Eu(III) content in the framework was significantly reduced by incorporation of Gd(III) ion.

Here we report the synthesis, single-crystal structure determination, topological analysis, characterization by thermal analysis and powder thermogravimetry of three novel compounds based on psa, with formula [Ln₂(C₁₀H₈O₄)₃(H₂O)] with Ln(III) = Sm, Eu, Eu-Gd. The PL properties of these compounds are presented and discussed in comparison with those of other related REE-MOFs. The characterization by Scanning Electronic Microscopy (SEM) and Atomic Force Microscopy (AFM) of samples resulting from miniaturization-exfoliation assays along with the corresponding luminescence activity are also reported.

2. Experimental Section

2.1. Synthesis

2.1.1. GENERAL PROCEDURES FOR SYNTHESIS OF [Sm₂(C₁₀H₈O₄)₃(H₂O)] (Sm-psa) AND [Eu₂(C₁₀H₈O₄)₃(H₂O)] (Eu-psa). Both compounds were synthesized under identical solvothermal conditions, by dissolving 2-phenylsuccinic acid (1 mmol) and the lanthanide chlorides (1 mmol) in a mixture of 30 mL of distilled water and 30 mL of ethanol. The pH value was adjusted to 3-4.5 with 1 mmol of 4,4'-bipyridine. The resultant mixtures were heated at 160 °C in a 120 mL Teflon-lined Parr bomb during three days and then, the reactor was immediately cooled to room temperature (42% and 39% yields based on Sm and Eu, respectively). Anal. Calcd. for **Sm-psa**: C, 40.26; H, 2.9; O, 23.23. Found: C, 40.32; H, 2.71; O, 23.30. Anal. Calcd. for **Eu-psa**: C, 40.12; H, 2.89; O, 23.14. Found: C, 40.11; H, 2.69; O, 23.22.

2.1.2. GENERAL PROCEDURE FOR SYNTHESIS OF [Eu_{1.11}Gd_{0.89}(C₁₀H₈O₄)₃(H₂O)] (Eu,Gd-psa). The compound was prepared under the same solvothermal conditions (temperature, reaction time, pH value and solvent mixture) as **Eu-psa** and **Sm-psa**, by dissolving 2-phenylsuccinic acid (2 mmol) and the lanthanide chlorides with a 0.75:0.75 molar ratio. The molar ratio of Eu(III)/Gd(III) in the mixed compound was determined by Inductively Coupled Plasma Mass Spectrometry (ICP-MS) (45% yield based on Eu). Anal. Calcd. for **Eu,Gd-psa**: C, 39.91; H, 2.88; O, 23.02. Found: C, 39.84; H, 2.81; O, 22.92.

Colorless rhombic single crystals suitable for X-ray diffraction were obtained for all the compounds.

2.1.3. MINIATURIZATION-EXFOLIATION ASSAYS. The **Eu-psa** samples with reduced particle size were obtained by the same synthesis route employed for **Eu-psa** with the addition of different amounts of sodium acetate (NaOAc). **Eu-psa-1**, **Eu-**

psa-2, **Eu-psa-3** and **Eu-psa-10** samples were obtained with 1 mmol, 2 mmol, 3 mmol and 10 mmol of NaOAc, respectively. The liquid exfoliation experiments of **Eu-psa-10** consisted in ultrasonication of suspensions prepared with two different concentrations; i.e. 5.46 mg or 0.28 mg of the crystalline sample in 1 mL ethanol, for a period of 60 minutes. The most concentrated mixture resulted in a milky white suspension, while an almost transparent colloidal solution was obtained with the most diluted one. The purity of the samples was confirmed by comparison of the experimental and simulated PXRD patterns (see Figure S1). Detailed information about the synthetic procedure and characterization is available in the Electronic Supplementary Information (ESI).

2.2. SINGLE-CRYSTAL STRUCTURE DETERMINATION. Single crystal of **Sm-psa** compound was mounted on a Bruker four circle kappa-diffractometer equipped with a Cu INCOATEC microsource operated at 30 W power (45 kV, 0.60 mA) to generate Cu K α radiation ($\lambda = 1.54178 \text{ \AA}$), and a Bruker AXIOM area detector (microgap technology). Diffraction data were collected over a hemisphere of reciprocal space in a combination of phi and omega scans to reach a resolution of 0.8 \AA (58.91 $^\circ$ in θ), using a Bruker APEX2 software suite (each exposure of 10 s covered 0.5 $^\circ$ in ω).

Single crystals of **Eu-psa** and **Eu,Gd-psa** compounds were mounted on an Agilent Gemini A four circle kappa-diffractometer equipped with an enhance Mo X-ray source operated at 2 kW power (50 kV, 40 mA) to generate Mo K α radiation ($\lambda = 0.71073 \text{ \AA}$), and a Agilent EOS area detector. Diffraction data were collected employing omega scans to reach a resolution of 0.8 \AA (29.1 $^\circ$ in θ), using a CrysAlisPro software suite (each exposure of 100 s covered 1 $^\circ$ in ω). **Eu-psa** was measured at low temperature (170K) with an Oxford Cryosystem Desktop Cooler.

Unit cell dimensions were determined by a least-squares fit of reflections with $I > 2\sigma(I)$. A semiempirical absorption and scale correction based on equivalent reflection was carried out using SADABS²⁶. Space group determinations were carried out using XPREP²⁷. The structures were solved by direct methods and refined by anisotropic full-matrix least-squares using SHELXL-2014²⁸. A summary of the conditions for data collection and structure refinement is given in Table 1. The coordinated water hydrogen atoms were refined using constraints. All calculations were performed using the following: SMART software for data collection; SAINT plus program²⁹ for integration and scale correction of data; SHELXTL²⁶ to resolve and refine the structure and to prepare material for publication; and ATOMS³⁰ and MERCURY 2.0³¹ for molecular graphics.

2.3. POWDER X-RAY DIFFRACTION (PXRD). X-ray powder diagrams were obtained with a Rigaku D-MAX-IIIC diffractometer using Cu K α radiation ($\lambda=1.5418 \text{ \AA}$) and NaCl and quartz as external calibration standards. The best counting statistics were achieved using a scanning step of 0.02 $^\circ$ between 5 $^\circ$ and 60 $^\circ$ Bragg angles with an exposure time of 5 s per step.

2.4. THERMODIFFRACTOMETRY. Thermodiffractometry measurements were performed in a Panalytical X'pert PRO

$\theta/2\theta$ geometry diffractometer with a Johansson monochromator, using Cu K α radiation.

2.5. THERMAL ANALYSIS. Thermogravimetric Analysis (TGA), Differential Thermal Analysis (DTA) and Differential Scanning Calorimetry (DSC) were performed with Shimadzu TGA-51, DTA-50 and DSC-60 apparatus under flowing air at 50 mL min⁻¹, and a heating rate of 10 $^\circ\text{C min}^{-1}$. X-ray powder diffraction was applied for further characterization of the pyrolysis products.

2.6. SCANNING ELECTRON MICROSCOPY (SEM). The images were obtained on Zeiss LEO1450VP equipment and Energy Dispersive Analysis of X-ray Spectroscopy (EDS) study was performed on an EDAX Genesis 2000 (see Figure S2). Samples were placed on an adhesive carbon tape coated with gold.

2.7. ATOMIC FORCE MICROSCOPE (AFM). The measurements were acquired using a Digital Instruments Multimode AFM with Nanoscope III controller. AFM images were acquired in Tapping mode with all parameters including set-point, scan rate and feedback gains adjusted to optimize image quality and minimize the force between the probe and sample. The **Eu-psa-10** particles present in the ultrasonicated ethanolic suspensions were collected and dispersed by drop casting the colloidal suspensions onto a glass flat substrate for characterization under AFM.

2.8. SOLID STATE LUMINESCENCE MEASUREMENTS. The steady state and time resolved luminescence measurements were done on a double Edinburgh Instruments FLSP920/FSP920 spectrometer setup, using a 450W xenon lamp as the steady state excitation source and a 60W pulsed xenon lamp as the time resolved excitation source (operating at a pulse frequency of 100 Hz for the europium samples). The emission was detected by a Hamamatsu R928P photo multiplier tube, sensitive between 200 and 900 nm. Excitation spectra were corrected for the xenon lamp emission profile, whereas emission spectra were corrected for the detector response curve. All measurements were carried out at a step size of 0.1 nm.

2.9. FOURIER TRANSFORM INFRARED SPECTROSCOPY (FTIR) AND VARIABLE TEMPERATURE FOURIER TRANSFORM INFRARED SPECTROSCOPY (VT-FTIR). FTIR spectra were recorded with a Nicolet Protégé 460 spectrometer in the 4000–225 cm⁻¹ range with 64 scans and a spectral resolution of 4 cm⁻¹ by the KBr pellet technique. For the **Eu-psa** compound, a variable-temperature cell was required.

3. Results and discussion

3.1. Crystal structures of Ln(III)-psa compounds

The structural description is based on the single-crystal data of the **Eu-psa** compound and specific information about the **Sm-psa** one will be given when necessary.

There are two crystallographically nonequivalent Ln(III) ions and three psa ligands in the asymmetric unit of the compound. The Ln1 ions are surrounded by eight oxygen atoms, all coming from carboxylate groups, while the Ln2 ones are

nonacoordinated through eight oxygen atoms from carboxylate groups and the remaining one from the coordinated water molecule (see Figure 1-left). The coordination polyhedra geometry of Ln1 ions can be described as triangulated dodecahedra while the corresponding geometry for the Ln2 ones is consistent with a monocapped square antiprism. The bond lengths fall in the range 2.296(6)- 2.638(6) Å for [Eu1O₈] and between 2.310(7) and 2.656(7) for the [Sm1O₈] polyhedra; the bond distances for the [Eu2O₉] and [Sm2O₉] ones are 2.372(6)-2.605(6) Å and 2.382(7)-2.630(6), respectively.

Table 1: Crystallographic data for **Sm-psa**, **Eu-psa** and **Eu,Gd-psa** compounds.

	Sm-psa	Eu-psa	Eu,Gd-psa
crystal system	monoclinic	monoclinic	monoclinic
empirical formula	Sm ₂ C ₃₀ H ₂₆ O ₁₃	Eu ₂ C ₃₀ H ₂₆ O ₁₃	Eu _{1.11} Gd _{0.89} C ₃₀ H ₂₆ O ₁₃
formula mass	895.21	898.43	903.72
space group	P2 ₁ /c	P2 ₁ /c	P2 ₁ /c
a [Å]	15.3688(8)	15.1320(9)	15.3112(7)
b [Å]	18.2815(9)	18.0343(13)	18.1174(6)
c [Å]	11.1221(5)	11.0712(5)	11.0982(5)
α [°]	90.00	90.00	90.00
β [°]	101.222(3)	100.430(5)	100.778(5)
γ [°]	90.00	90.00	90.00
V [Å ³]	3065.2(3)	2971.3(3)	3024.3(2)
ρ _{calcd} [g.cm ⁻³]	1.940	2.006	1.983
Temp (K)	296(2)	170(2)	293(2)
Z	4	4	4
F(000)	1736	1744	1748
abs coeff [mm ⁻¹]	29.058	4.252	4.296
Crystal size [mm]	0.18x0.08x0.04	0.23x0.11x0.05	0.12x0.10x0.03
T _{min} /T _{max}	0.0776/0.3894	0.072/0.306	0.60/0.88
index ranges			
h	(-17,16)	(-19,20)	(-20,20)
k	(-20,13)	(-24,18)	(-24,24)
l	(-11,12)	(-14,14)	(-14,14)
reflns	4709/3408	14326/6851	10091/9046
collected/unique with I>2σ(I)			
abs corr	semiempirical	Empirical	empirical
refined parameters	412	412	413
goodness-of-fit on F ²	1.036	1.067	1.154
refinement method	full-matrix least-squares on F ²	full-matrix least-squares on F ²	full-matrix least-squares on F ²
final R indices	R ₁ = 0.0529	R ₁ = 0.0565	R ₁ = 0.0583
λ [Å]	1.54178	0.71073	0.71073
[I > 2σ(I)]	wR ₂ = 0.1172	wR ₂ = 0.103	wR ₂ = 0.158
R-factor-all	0.0821	0.0893	0.0689

All psa ligands coordinate four metal ions and two of them (Types A and B) exhibit the same coordination modes, i.e. by a chelate-bridge mode by one carboxylate group and as bidentate-bridge by the other one. These ligands adopt a *gauche* conformation with dihedral angles C1A-C2A-C3A-C4A = -62.87° (Type A) and C1B-C2B-C3B-C4B = -51.87° (Type B) (for **Sm-psa** compound, Type A = 64.58°, Type B = -53.01°). A third ligand (Type C) presents a more complex coordination mode, connecting four adjacent Ln(III) through a chelate-bridge mode by one carboxylate extreme and a tridentate-bridge mode by the other one (see Figure 2-a). This ligand presents a torsion angle C1C-C2C-C3C-C4C = 65.18° for the **Eu-psa** compound and C3-C14-C13-C6 = 62.45° for the **Sm-psa** one.

The chelate-bridge carboxylate groups belonging to the three psa conformers are responsible for the metal-condensation leading to 1D secondary building units (SBUs) composed by infinite chains of edge-sharing polyhedra that run in zig-zag along the [001] direction. In these structures, the type A ligands are the real linkers since they connect the SBUs allowing the formation of the organic-inorganic bidimensional framework. The distance between adjacent Ln(III) ions inside the chain is 3.985 Å for those bonds involving Type B and C psa, whereas it is 4.006 Å for those formed by Type A and C ones (Figure 1-right).

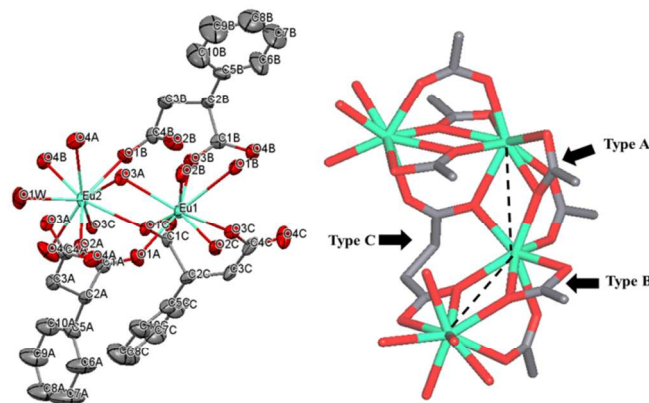


Figure 1: ORTEP drawing of the asymmetric unit for the **Eu-psa** compound (left) and detail of the SBU architecture (right).

As can be seen in Figure 3, the resultant framework is 2D covalently bonded with layers stacked in [100] direction through weak π - π interactions of type C-H \cdots C=C with an edge-orientation³²; the distances H \cdots C=C are in the range 3.3-3.9 Å.

These MOFs can be classified as I¹O¹ according to the classification proposed by Cheetham et al.³³

The coordinated water molecules are oriented towards the spaces delimited by the SBUs and although their hydrogen atoms could not be localized, a strong H-bond interaction

involving a carboxylate group should exist, since the distance $O1w \cdots O10$ is 2.685 Å.

The analysis of the crystal structure reveals that these MOFs are almost isomorphous with those of Er(III)^{13a} and Lu(III)^{13b} and the related 2,2-dimethylsuccinate (2,2-dms) ligand, corresponding to the $P2_1/c$ space group (S.G.) with cell parameters $a = 11.1794(5)$, $b = 18.2208(8)$, $c = 12.7944(6)$, $\beta = 112.4270(10)^\circ$ for the Er-compound, and $a = 11.1375(4)$, $b = 18.0442(5)$, $c = 12.7462(4)$, $\beta = 112.496(4)^\circ$ for the Lu-compound. The exact isomorphous character is not verified since there are subtle differences in the coordination modes of the 2,2-dms ligands in comparison with those of the psa ones (see Figure 2-b). Such differences lead to SBUs composed by 1D chains of alternating edge-sharing and vertex-sharing polyhedral in the related dms frameworks instead of all edge-sharing polyhedra as in the psa-based compounds. The incidence of two methyl substituents in the same carbon atom is comparable to the presence of one bulky phenyl group as substituent, since the resultant frameworks are almost identical. Moreover, in both types of nets a complex coordination mode can be identified (corresponding to the psa Type C ligand) called "malonate mode"^{13a} since this is frequent in malonate but unusual in longer aliphatic dicarboxylates.

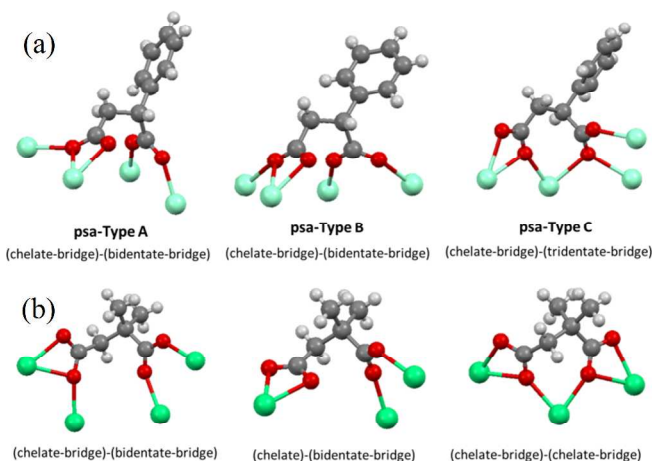


Figure 2: Representation of psa (a) and 2,2-dms (b) coordination modes.

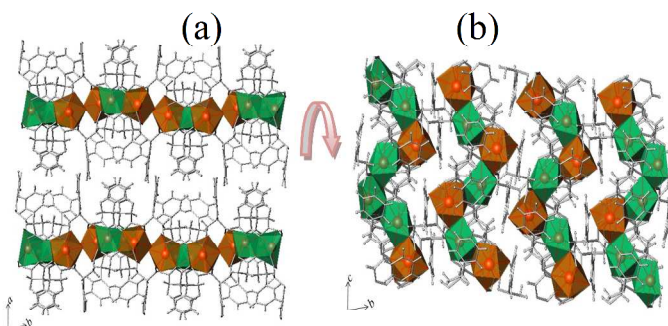


Figure 3: Projection on the ab (a) and cb (b) planes of Eu-psa.

Finally, the **Eu,Gd-psa** compound is isostructural to those containing all-Eu or all-Sm ions as can be verified by the single-crystal data displayed in Table 1.

Due to the fact that in this structure there are two different crystallographic sites for the Ln(III) ions, the structure was solved and refined twice exchanging the metal ion in each position in order to determine if each one occupies a unique crystallographic site or if they are disordered over the two sites. The anisotropic thermal displacement parameters of each lanthanide atom and the corresponding final R and wR refinement values did not show significant differences when the position of the Gd(III) ion was exchanged with the Eu(III) one. Thus, regarding the limitation of the XRD technique to distinguish atoms with similar scattering factors and considering the results obtained for the described solution/refinement procedure, the presence of both Ln(III) ions in both crystallographic sites seems to be the most appropriate structural model.

3.2. Topological analysis

The crystal structure of the Ln-psa compounds was analyzed with the TOPOS program³⁴ in order to determine the underlying topology³⁵ of the associated simplified net. To this end, the simplification procedure takes into account the fact that the SBU consists of infinite zig-zag chains. As can be seen in the sequence I-IV of Figure 4, the deconstruction process of each layer to obtain the corresponding simplified net can be understood as the extraction of the SBU (drawn in green) and the psa Type A (drawn in yellow). The topological roles of psa Type B and C (marked in gray) are not considered since they are only decorating the SBU. As a result, the simplified net can be described as a 3-connected uninodal **fes** type, *Shubnikov plane net*, Schläfli symbol $(4.8^2)^{36}$.

By the same method, the same topology can be obtained for the almost isomorphous compounds based on Er(III)^{13a} (or Lu(III)^{13b}) ions and the related 2,2-dms ligand. However, if a ghost atom is located on the centroid position between adjacent Ln(III) ions, another 3-connected net belonging to the **hcb** type (*Shubnikov hexagonal plane net*, Schläfli symbol (6^3)) is obtained, as it was recently reported in a highlight of REE MOFs³⁷. As can be seen from the comparison of **fes** and **hcb** topological types for all the Ln(III)-psa frameworks (Figure 5), the **fes** net describes better the 2D connectivity; besides, it can be obtained without any extra node (as requires the obtaining of the **hcb** type), which is preferred for simpler topological analysis procedures.

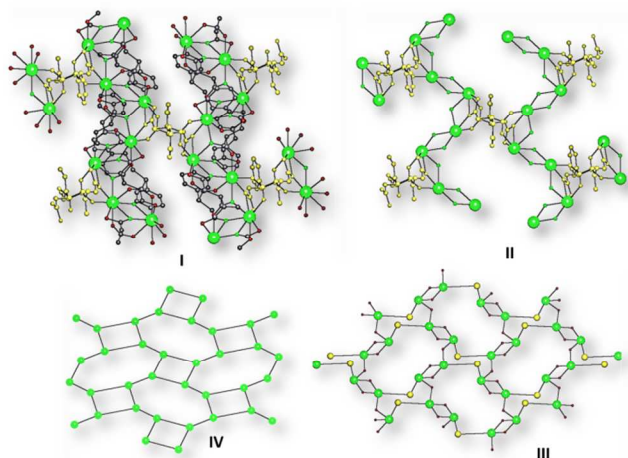


Figure 4: Schematic representation of the topological analysis based on the deconstruction of the Ln(III)-psa frameworks (I-III) leading to the **fes** type net (IV).

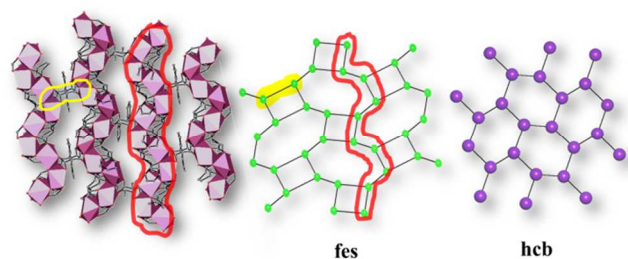


Figure 5: Comparison of the Ln(III)-psa frameworks with the **fes** and **hcb** nets.

3.3. Vibrational and Thermal analysis

The interpretation of the IR spectrum of the **Eu-psa** compound was performed by considering the most important internal vibrations of water molecules, carboxylate, methylene and phenyl groups and their comparison with those observed in **H₂psa** and related compounds^{38,39}. The assignment of these modes, particularly the librational ones, was performed by comparing the spectra of partially and completely dehydrated **Eu-psa** samples obtained with a VT-FTIR cell. The IR spectra for all the compounds are available in ESI (Figures S3 and S4). The band in the OH stretching zone is located at frequency values consistent with the presence of water molecules that are involved not only in coordination to a metal ion but also in hydrogen bonds in the lattice. In both spectra the bands located at 910, 725 and 645 cm^{-1} correspond to water librational modes since they are strongly affected with increasing temperature and totally disappear when dehydration takes place (Figure S3). The variety of coordination types exhibited by the carboxylate groups is evidenced in the splitting of their corresponding stretching modes. Two bands at 1595 and 1560 cm^{-1} are assigned to the $\nu_{\text{as}}(\text{OCO})$ whereas a pair of bands at 1415 and

1400 cm^{-1} are associated with the corresponding symmetric mode. Additionally, a component at higher frequency (1625 cm^{-1}) can be tentatively ascribed to the “malonate mode” derived from the *psa* Type C conformer. Several works dealing with metal malonate complexes that contain the six-membered ring originated in the mentioned mode, report this band as the spectroscopic evidence⁴⁰.

The $\nu(\text{CH})$ modes of the corresponding aromatic and aliphatic groups appear above and below 3000 cm^{-1} , respectively. The bands located at 1455 and 1435 cm^{-1} are assigned to $\delta(\text{CH}_2)$. Similar features regarding frequency values and intensities are found in the **Sm-psa** and **Eu,Gd-psa** spectra.

The thermal data for **Sm-psa**, **Eu-psa** and **Eu,Gd-psa** compounds are presented in ESI; the Δm % values calculated on the basis of the determined stoichiometries show a good agreement with the experimental ones. The corresponding TGA and DTA curves for **Eu-psa** are displayed in Figure 6a while Figures S5 and S6 show the curves for the remaining compounds.

The dehydration process is associated with a weak endothermic signal that is hardly detectable in the DTA curves but perfectly visible in the corresponding DSC experiments (Figure 6b and Figure S7). Thermal evolution proceeds with the decomposition of the organic linkers through three steps leading to the formation of the respective Ln_2O_3 . The corresponding mass decays are accompanied by strong exothermic DTA peaks.

According to the thermogravimetry experiments showed in Figure 6c, a slight expansion of the crystalline cell of **Eu-psa** is observed when heating up to the dehydration temperature. The recovering of the original structure once room temperature is reached again, demonstrates that the reversibility of the process is not fully complete. This fact is also supported by the DSC curves registered on a heating-cooling-heating cycle.

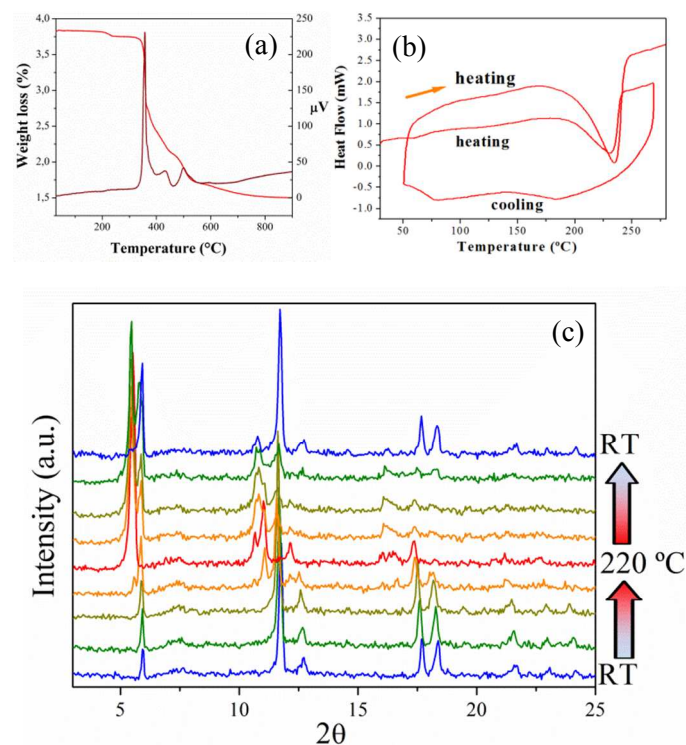


Figure 6: Thermal characterization and thermodiffraction experiments for **Eu-psa**. TGA-DTA curves (a), DSC curve involving the dehydration zone (b) and XRD patterns zoomed in the 2θ range 3° - 25° as a function of temperature (c).

3.4. Miniaturization-exfoliation experiments

Regarding the optical and magnetic properties of Ln-MOFs, their applications in thin film devices have received special attention during the last decade.⁴¹ The specific applications such as gas sorption⁴² and photoluminescence⁴³, depend greatly on the ability to control size and shape of individual crystallites as well as their assembly on various supporting surfaces.²³ The miniaturization of MOFs has already become one of the most prosperous disciplines in current chemistry of these compounds as it bridges the gap between fundamental MOF science and prospective applications.⁴⁴ Thus, it is very important to synthesize individual nanoscale Ln-MOF crystallites that are useful for film preparation.⁴⁵ Diverse techniques have been developed with the aim to produce nanometer-sized MOFs such as reverse microemulsion⁴⁶, microwave-assisted synthesis⁴⁷ and the use of capping agents.⁴⁸ Here, we used NaOAc as capping agent to reduce the crystal size of **Eu-psa** crystallites and represents, as far as we know, the first example of attempting miniaturization in Ln-succinate compounds.

In the absence of NaOAc, **Eu-psa** crystals exhibit an average length of $\sim 182 \mu\text{m}$ (Figure 7a). Increasing amounts of the salt lead to changes both in crystal shape and size. The formation of aggregates composed by capped crystals, whose sizes are almost half of the original ones, becomes clear in the presence of 3 mmol NaOAc (Figure 7b-c). Finally, when 10 mmol NaOAc are added to the conventional synthesis, the formation of *quasi* rounded particles of 43 μm diameter composed by stick-shaped crystals with thickness ranging 700 - 800 nm and lengths about 6 μm is observed (Figure 7d). The nature of these samples was investigated by PXRD and FTIR techniques (Figures S8 and S9) confirming the presence of a unique phase consistent with the bulk one (**Eu-psa**). Extra unknown phases occur with the addition of more than 10 mmol NaOAc (i.e. 15 and 20 mmol).

As it was described in section 2.1.3., the surface topography of the exfoliated nanosheets was characterized by means of AFM, while PXRD and FTIR measurements determined that no modifications occur in relation to the bulk phase (Figure S10 and S11). The PXRD pattern of the exfoliated **Eu-psa-10** sample shows a strong preferred orientation of the (100) and (200) crystallographic planes that result statistically more exposed by deposition of the obtained nanolayers. This is an expected fact since exfoliation can only take place through that direction in which non-covalent interactions ensure the packing of the layers (see Figure S12). We found that the **Eu-psa-10** framework present in the 0.28 mg mL^{-1} ethanolic suspension was partly exfoliated to a thickness of around 20 nm, corresponding to ~ 20 elementary host layers, while retaining lateral dimensions of up to 0.5 μm (see Figure 8). Delamination of the crystals in the suspension containing a higher

concentration (5.46 mg mL^{-1}) occurs in a less extent, leading to wider nanolayers of $\sim 50 \text{ nm}$ thickness, showing the concentration of the sonicated suspension is an important factor to consider in order to achieve a controlled exfoliation degree.

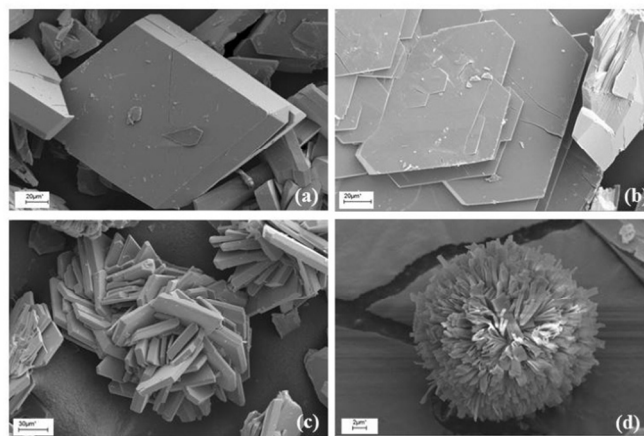


Figure 7: SEM micrographs of **Eu-psa-1** (label scale 20 μm) (a), **Eu-psa-2** (label scale 20 μm) (b), **Eu-psa-3** (label scale 30 μm) (c) and **Eu-psa-10** (label scale 3 μm) (d).

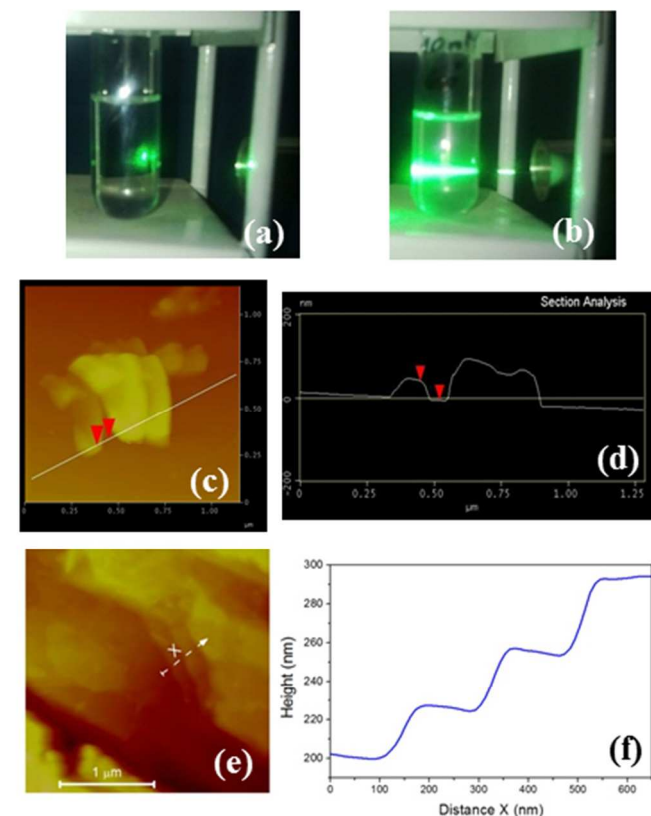


Figure 8: Demonstration of the Tyndall effect in colloidal suspensions containing exfoliated nanolayers of **Eu-psa-10**. The path of the green laser beam is invisible in pure ethanol (ignoring reflections by the glass surfaces) (a). The laser beam is clearly visible through a colloidal solution comprising 0.28 mg of **Eu-psa-10** particles suspended in 1 mL ethanol (b). AFM 2D height image of the nanolayers, obtained by sonication of an ethanolic suspension containing 8.2 mg mL^{-1} of **Eu-**

ARTICLE

psa-10 (c) and the height profile along the marked distance (d). Bidimensional AFM image corresponding to exfoliated nanosheets present in an ethanolic suspension of 0.28 mg mL⁻¹ of **Eu-psa-10** ultrasonicated sample (e) and the corresponding height profile along the marked X distance (f).

3.5. Luminescence properties

According to a significant number of specialized articles⁵, the PL properties of materials can be characterized by the following measurements: 1) luminescence spectra, defined as intensity as a function of wavelength [$I = f(\lambda)$], 2) quantum yield (Q), which gives the efficiency of the luminescence process and is defined as the ratio of the number of emitted photons released in the process of luminescence to the number of absorbed photons, and 3) observed lifetime (τ_{obs}) which refers to the average time the molecule stays in its excited state before emitting a photon and is determined as being inversely proportional to the sum of the rate constants of the radiative (k_r) and the nonradiative (k_{nr}) processes:

$$\tau_{\text{obs}} = 1/(k_r + k_{nr}) \quad (1)$$

In the present section, the PL properties of **Sm-psa** and **Eu-psa** compounds are presented and discussed in terms of their emission spectra and lifetimes. Moreover, a deeper analysis of such properties for the Eu(III) ions in different crystallographic environments was also performed by comparison with the corresponding features of the related **Eu-2,3-dms**, [Eu₂(C₆H₈O₄)₃(H₂O)₂]^{13c} 3D framework. Finally, the PL performance of **Eu-psa** samples with reduced particle size with and without exfoliation treatment was evaluated.

Upon excitation at 402.5 nm, in the ⁴L_{13/2}, ⁶P_{3/2}, ⁴F_{7/2} ← ⁶H_{5/2} transitions (Table S1), the **Sm-psa** shows the typical Sm(III) emission peaks (Figure 9) at 561.7, 597.8, 644.7 and 705 nm, which have been assigned to the corresponding electronic transitions in Table S2. No peaks were visible in the NIR range for this sample. Similar features were found for the **Sm-2,3-dms** compound previously reported^{13c}. The CIE (Commission Internationale de l'Éclairage) chromaticity diagram showing the luminescence color is displayed as an inset in Figure 9. The corresponding luminescence decay profile is given in Figure S13 from which it can be seen that the experimental curve fits satisfactorily with a mono-exponential decay. The calculated lifetime (τ) is 3.50 μs.

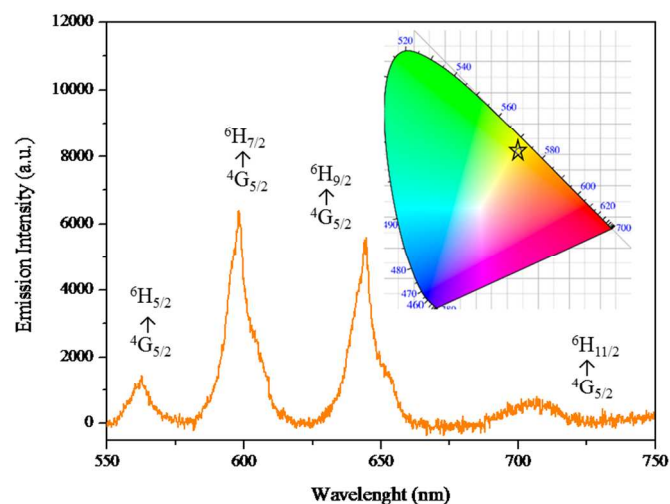


Figure 9: Emission spectrum of **Sm-psa** compound. The inset shows the corresponding CIE diagram with the chromaticity coordinates x,y (0.47, 0.51).

All the Eu-MOFs under the present study show the typical europium-based luminescence. The emission spectra for **Eu-psa** and **Eu-2,3-dms** are given in Figure 10 and the assignment of the observed electronic transitions can be found in Table S3. Figure S14 shows the excitation spectra of the **Eu-2,3-dms**, **Eu-psa**, **Eu,Gd-psa** and **Sm-psa** compounds. A weak underlying broad band at short wavelengths is visible in the excitation spectra of **Eu-psa** and **Eu,Gd-psa**, most likely originating from the $\pi^* \leftarrow \pi$ or $\pi^* \leftarrow n$ transitions from the psa linkers. The most intense peaks in the spectrum, however, correspond to transitions within the Eu(III) ion's 4f shell. In the case of **Eu-2,3-dms**, all peaks correspond to transitions within the Eu(III) ion's 4f shell. This fact suggests that hardly any "antenna effect"⁵ is observed in these compounds. As a result, the luminescence shown by the Eu-MOFs can be obtained by exciting the lanthanide ion directly in its ^{2S+1}L_J electronic energy levels, provided that these are at high enough energy to allow the lanthanide-centered luminescence. The corresponding assignment of the 4f-4f excitation transitions for the Eu-MOFs is presented in Table S4.

Upon excitation at 393.5 nm for **Eu-psa** and 393.3 nm for **Eu-2,3-dms**, the typical Eu(III) emission is obtained, and the emission peaks of the compounds correspond to the transitions from ⁵D₀ → ⁷F_J ($J = 0-6$) in the 550 - 850 nm range. Among these emission lines, the most striking red emission derives from the ⁵D₀ → ⁷F₂ transition in both Eu-MOFs emission spectra.

When the peaks labeled "a" in the emission spectra are magnified only one peak can be seen. As this peak corresponds to a transition between two non-degenerate energy levels, there can only be one peak present in the spectra when only one crystallographic site is present, as this peak cannot be split by the crystal field. This would therefore suggest only one independent crystallographic Eu(III) site. This is in agreement with the crystallographic data that determines two nearly

identical sites in **Eu-2,3-dms** structure (triclinic, Pt S.G.) where the Eu(III) ions are nine-coordinated by eight oxygen atoms coming from carboxylate groups and the remaining one from a coordinated water molecule; however, the emission spectrum does not reflect the presence of two different crystallographic environments in **Eu-psa** (Figure 10). It should be mentioned that inequivalent but similar coordination environments can give rise to very comparable $^5D_0 \rightarrow ^7F_0$ peaks, which can overlap and be seen as one peak.

Table 2 lists the luminescence decay times that have been recorded for both Eu-compounds. The decay traces can be found in Figures S13. When two crystallographic environments are different enough, it is assumed that each Eu(III) ion would have its own decay profile, leading to the necessity of two exponential terms to fit the decay curve. For **Eu-2,3-dms**, the decay curve can be satisfactorily fitted with a single exponential function with $\tau_{\text{obs}} = 0.520$ ms, in agreement with the near identical nature of the Eu coordination environments in this material. The luminescence decay profile of **Eu-psa** however shows a biexponential behavior yielding lifetimes values of $\tau_1 = 0.533$ ms (91.5%) and $\tau_2 = 1.171$ ms (8.5%) with an average luminescence decay time calculated from the biexponential fit $\tau_{\text{ave}} = 0.587$ ms. This reflects the presence of two sufficiently different Eu coordination environments in this material.

The ratio between the intensity of the $^5D_0 \rightarrow ^7F_2$ and the $^5D_0 \rightarrow ^7F_1$ transitions $[R = I(^5D_0 \rightarrow ^7F_2) / I(^5D_0 \rightarrow ^7F_1)]^{5c}$ is another interesting parameter that allows to relate the PL properties with the structural features. As it was mentioned above, the strongest emission in these compounds is assigned to the $^5D_0 \rightarrow ^7F_2$ hypersensitive transition, which is an electric dipole transition. The hypersensitive nature of this specific transition translates into a greater sensitivity to the crystal field symmetry of the coordination sphere of the Eu(III) ion. In contrast, the $^5D_0 \rightarrow ^7F_1$ transition is a magnetic dipole one and its intensity is virtually independent of the environment of the Eu(III) ion. The higher this ratio R, the more intense the red emission of the $^5D_0 \rightarrow ^7F_2$ transition and the lower the symmetry of the Eu(III) environment. As can be observed in Table 2, the R value for **Eu-psa** is higher than that of **Eu-2,3-dms**, thus indicating a more asymmetric environment around the Eu(III) ions in the former compound. Thus, it is noteworthy that the luminescence decay profile features as well as the R values are in good agreement with the crystallographic data in both cases.

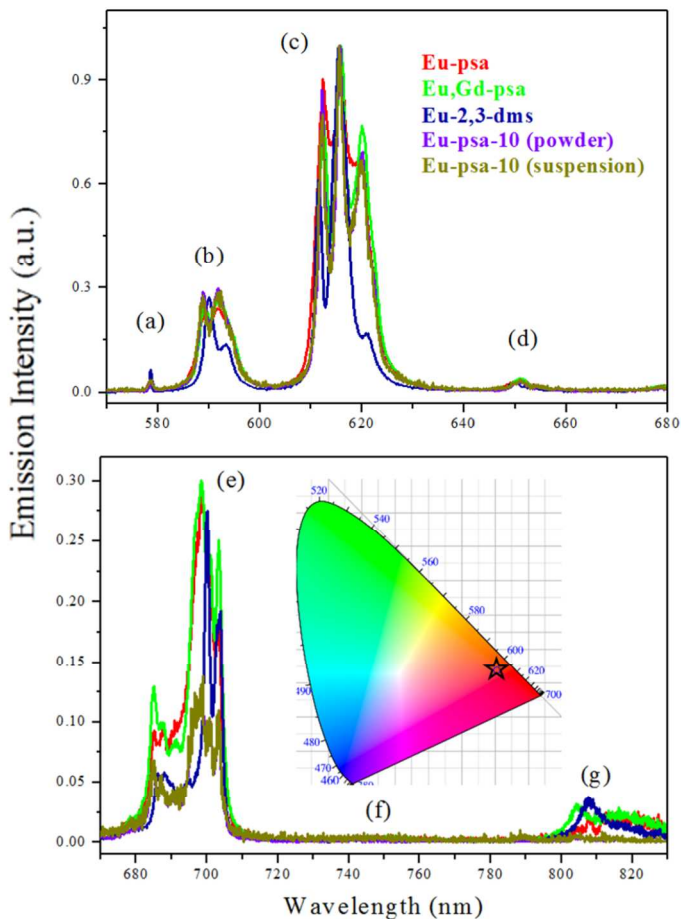


Figure 10: Emission spectra of Eu-compounds in the 570 to 680 nm (top) and 670 to 830 nm (bottom). The inset shows the corresponding CIE diagram with the chromaticity coordinates x, y for **Eu-psa** (0.66, 0.34).

For a correct evaluation of the PL efficiency of both Eu-MOFs, the intrinsic quantum yields (Q_{Ln}) were calculated (see Table 2). This parameter, along with the efficiency of sensitization, determines the overall luminescence quantum yield (Q).

Assuming that non radiative and radiative processes are essentially involved in the depopulation of the 5D_0 state, the Q_{Ln} can be expressed as:

$$Q_{Ln} = k_r / (k_r + k_{nr}) \quad (2)$$

Thus, Q_{Ln} of the luminescence expresses how well the radiative processes compete with the non-radiative processes described by eqn. (2). In general, contributions of the k_{nr} include back-energy transfer to the sensitizer, electron transfer quenching and quenching by matrix vibrations. Moreover, vibrations commonly found in organic molecules (C-H, O-H, N-H) can have important contributions to k_{nr} .⁴⁹ The radiative contribution k_r can be calculated from the equation:

$$k_r = 1 / \tau_{\text{rad}} \quad (3)$$

The so-called radiative lifetime τ_{rad} can be approximated for Eu(III) by the equation⁵⁰:

$$k_r = (1/\tau_{\text{rad}}) = A_{\text{MD},0} \cdot n^3 \cdot (I_{\text{tot}}/I_{\text{MD}}) \quad (4)$$

Here, $A_{\text{MD},0}$ is the spontaneous emission probability of the ${}^5\text{D}_0 \rightarrow {}^7\text{F}_1$ magnetic dipole transition equal to 14.65 s^{-1} , n is the refractive index (1.5), I_{tot} is the total integrated emission of the ${}^5\text{D}_0 \rightarrow {}^7\text{F}_J$ ($J=0-6$) transitions and I_{MD} is the integrated emission of the ${}^5\text{D}_0 \rightarrow {}^7\text{F}_1$ transition.

If the radiative lifetime, τ_{rad} , is known, Q_{Ln} can be calculated using the observed luminescence lifetime. Basing on eqn. (1) and (4), the intrinsic quantum yield can be calculated as:

$$Q_{\text{Ln}} = \tau_{\text{obs}}/\tau_{\text{rad}} \quad (5)$$

At the same time, knowledge of both τ_{obs} and τ_{rad} enables determination of the overall rate of non-radiative deactivation. Hence, the radiative lifetime is an important parameter in the photophysical description of lanthanide luminescence. Considering that not much is known about the PL parameters of europium ions in MOFs, k_r , k_{nr} , and $Q_{\text{Ln}}\%$ for the Eu-compounds reported here are summarized in Table 2.

The fact that the $Q_{\text{Ln}}\%$ for **Eu-2,3-dms** is lower than the respective value for **Eu-psa** could be explained in terms of the water content, since high frequency vibrations of water molecules contribute efficiently to the quenching of the ${}^5\text{D}_0$ luminescence. The former compound exhibits two water molecules per asymmetric unit instead of only one in the latter one. In addition, high concentration of metallic centers is also detrimental for the luminescence efficiency through cross-relaxation and energy transfer processes. Then, the so-called *concentration quenching of the luminescence*, should be more marked in the 3D **Eu-2,3-dms** where the inorganic chains are separated by 5.9 \AA along the b direction (via the *gauche*-dms ligands) and 9.5 \AA along the c direction (via the *trans*-2,3-dms anions). The **Eu-psa** framework exhibits layers containing chains of polyhedra spaced by 7.368 \AA ; in turn, a higher distance of 15.42 \AA separates successive layers, as previously described in the crystallographic section.

Table 2: Photophysical parameters of the Eu-MOFs [*]

	R	$\tau_{\text{obs}}(\text{ms}) \pm \text{SE}^{**}$	τ_{rad} (ms)	k_r (s^{-1})	k_{nr} (s^{-1})	Q_{Ln} %
Eu-2,3- dms	4.4	0.515 \pm 0.004(6)	2.64	379	1562	19.5
Eu-psa	4.7	0.587 \pm 0.002(7)	2.59	386	1318	22.6
Eu-psa-10 (suspension)	3.5	0.834 \pm 0.001(9)	4.76	210	989	17.5
Eu-psa-10 (powder)	3.4	0.848 \pm 0.001(4)	3.73	268	911	22.7
Eu,Gd-psa	4.0	0.872 \pm 0.0009(2)	2.68	373	774	32.5

* The intrinsic quantum yields Q_{Ln} have been calculated using equations (2) to (5). Each τ_{obs} measurement was performed by triplicate. **SE: standard error.

The PL performance of an ethanolic suspension containing the miniaturized and further exfoliated **Eu-psa-10** sample (**Eu-psa-10** suspension) was investigated and compared with the corresponding one of the miniaturized - non exfoliated powder sample. The emission spectra of these samples are displayed in Figure 10, a detailed comparison is shown in Figure S15 and the corresponding excitation spectra are depicted in Figure S16. The assignment of the electronic transitions corresponding to the excitation and emission spectra are found in Tables S5 and S6, respectively, while their photophysical parameters are displayed in Table 2.

The relative intensities and splitting of the transition peaks are very similar in the emission spectra of **Eu-psa-10** (suspension) and **Eu-psa-10** (powder). The spectra feature the well-known Eu(III)-centered luminescence except for the ${}^5\text{D}_0 \rightarrow {}^7\text{F}_5$ transition which is occasionally visible at around 750 nm but cannot be detected in these spectra. In addition, the ${}^5\text{D}_0 \rightarrow {}^7\text{F}_6$ transition peak which appears at 807.4 nm is not visible in the emission spectrum of the suspension. The ${}^5\text{D}_0 \rightarrow {}^7\text{F}_0$ peak shows two components in the spectra of these samples, this fact being an interesting difference to remark with respect to the **Eu-psa** in the bulk form.

The $Q_{\text{Ln}}\%$ for **Eu-psa** and **Eu-psa-10** (powder) are similar, thus indicating that this parameter is not affected at least with this degree of particle size reduction. However, if the rate constants of deactivation processes or non-radiative de-excitation (k_{nr}) of **Eu-psa-10**, both in suspension and powdered phases, are compared, a significant decrease is observed with respect to that of the **Eu-psa** sample. This fact may be a consequence of the diminution in the particle size and consequent increase of the ratio of Eu ions at the surface with respect to Eu ions lying inside the particule, which in turn reduces the proportion of ions possessing in their immediacy other ones that can quench the luminescence. In other words, by decreasing the particle size, a certain reduction of the concentration quenching is achieved. Furthermore, if the **Eu-psa-10** (suspension) and **Eu-psa-10** (powder) i.e. exfoliated and not exfoliated, respectively, are compared, it is observed that the first one has a slightly higher k_{nr} value, this being probably due to the fact that in the interface layer-solvent, there are ethanol molecules that can interact with the ions at the surface and partially deactivate their emission through vibronic mechanisms involving the OH groups of the solvent⁵¹. The value of the $Q_{\text{Ln}}\%$, being dependent on the refractive index, seems not to reflect the improvement reached with miniaturization-exfoliation experiments. Even though it is out of the scope of this article, on the basis of these results, we think that obtaining **Eu-psa** nanolayers exhibiting promising luminescent parameters, suggests that a thin film obtained from their deposition could exhibit a luminescence performance at least comparable to that of the bulk material, but having the advantage of being suitable to be incorporated into optical devices. Studies of thin film

preparation by deposition of these Ln-psa nanolayers will be the focus of future research, since the preliminary results are quite auspicious.

Another approach to evaluate the impact of the *concentration quenching*, consisted in replacing 44.5% of the Eu(III) amount by Gd(III) ion to avoid the transfer of energy between Eu(III) centers, resulting in the mixed compound **Eu,Gd-psa**. Moreover, the Gd(III) also acts as a sensitizing ion for the Eu(III) ones⁵². As it can be noted in Table 2, the Q_{Ln} % and the lifetime, notably increase for **Eu,Gd-psa** whereas its k_{nr} value is less than that observed for all the **Eu-psa** samples, suggesting that an efficient avoidance in the electron transfer quenching between Eu(III) centers was achieved. The corresponding emission spectrum is presented in Figure 10. It has been shown before that Gd(III) codoping in luminescent lanthanide materials can lead to a significant increase in the (intrinsic) quantum yield of the codoped materials.⁵³

As it was already mentioned, despite only a few works dealing with a complete report of PL parameters for Eu-MOFs are found in the literature, a suitable comparison can be performed on the basis of the PL reported by Gai et al^{54, 55} for Eu-MOFs containing aromatic tetra- or hexacarboxylic acids as ligands. In this paper, the obtained Q_{Ln} % decreases from 20 to 10 as the ratio coordinated water/metal ion increases from 0.5 to 4, due to the deactivation process caused by the OH oscillators, as could be expected. In comparison, our results are especially promising for the **Eu,Gd-psa** compound, as not only the *concentration quenching* but also the presence of coordinated water in the inner sphere could be avoided.

Moreover, if both strategies are combined, i.e. miniaturization-exfoliation and direct replacement experiments, a highly promising layered material for thin films development can be easily obtained. We demonstrate here that by reducing the efficiency of the non-radiative pathways, an increase in the luminescence lifetime and quantum yields should be expected.

Conclusions

The reaction between Ln(III) ions (Sm, Eu and Eu-Gd) and 2-phenylsuccinic acid under solvothermal conditions led to new isostructural MOFs featuring 2D bonded layers composed by infinite zig-zag chains of octa- and ninecoordinated Ln polyhedra. The layered nature of these frameworks makes them suitable for their exfoliation in nanolayers. Miniaturization assays using sodium acetate as capping agent, and further exfoliation via ultrasonication were successfully carried out for the Eu(III) phase. Scanning electron microscopy confirms a diminution of the particle size of ~ 96% after miniaturization experiments with 10 mmol of the capping agent, leading to an average crystal length of ~ 6 μ m. This procedure also modifies the morphology of the bulk crystals resulting in *quasi* rounded aggregates composed by stick-shaped smaller crystals. The ethanolic suspension containing the mentioned miniaturized sample shows after ultrasonication, the characteristic Tyndall effect associated with colloidal systems. According to the

atomic force microscopy measurements, the rod-shaped crystals were readily separated into nanolayers ranging from about 20 to 50 nm. The PL measurements demonstrate a lanthanide-centered luminescence by direct excitation in their $2S+1L_J$ electronic energy levels without evidence of “antenna effect”. The PL properties of the bulk materials are consistent with the structural findings. Non-radiative processes in the **Eu-psa** were efficiently reduced either by partial replacement of the emitting centers by the sensitizing Gd(III) ion or through the miniaturization-exfoliation procedure. This fact is reflected in a higher intrinsic quantum yield in the former case and in a longer luminescence lifetime for the second one. The combination of both strategies seems to be a promising method for synthesizing and exploration of highly photoluminescent lanthanide-organic frameworks and can be considered as an interesting possibility for preparing thin films for optical devices.

Acknowledgements

This work was supported by the Consejo Nacional de Investigaciones Científicas y Técnicas (PIP CONICET 112-201101-00912); ANPCyT PICT-2012-1994 and Universidad Nacional de San Luis (PROICO 2-1612) G.E. Gomez thanks a Ph.D. CONICET fellowship. R.V.D. thanks the Hercules Foundation (project AUGÉ/09/024 “Advanced Luminescence Setup”) and Ghent University (UGent; project BOF 01N01010) for funding. G.E.N and M.C.B are members of CIC-CONICET.

Notes and references

^a Instituto de Investigaciones en Tecnología Química (INTEQUI). Area de Química General e Inorgánica “Dr. G.F. Puelles”, Facultad de Química, Bioquímica y Farmacia, Chacabuco y Pedernera, Universidad Nacional de San Luis, 5700 San Luis, Argentina. E-mail: gnarda@unsl.edu.ar.

^bGerencia de Investigación y Aplicaciones, Centro Atómico Constituyentes, Comisión Nacional de Energía Atómica, Av. Gral. Paz 1499, 1650 San Martín, Buenos Aires, Argentina.

^c L³ – Luminescent Lanthanide Lab, f-element coordination chemistry, Ghent University, Department of Inorganic and Physical Chemistry, Krijgslaan 281, Building S3, 9000 Gent, Belgium.

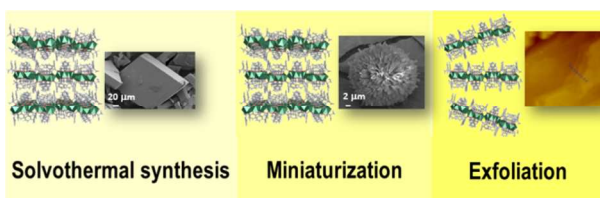
^d Instituto de Física Aplicada (INFAP-CONICET). Facultad de Ciencias Físico, Matemáticas y Naturales. Universidad Nacional de San Luis, Dpto. de Física, 5700 San Luis, Argentina.

† Electronic Supplementary Information (ESI) available: Crystallographic data in CIF format, synthesis details, powder XRD patterns, TG-DTA-DSC curves, FTIR spectra, excitation spectra, lifetimes curves and assignments tables of absorption and emission transitions. CCDC reference numbers 1002152, 1002153 and 1002154 contain crystallographic data for this paper. These data can be obtained free from the Cambridge Crystallographic Data via www.ccdc.cam.ac.uk/data_request/cif. See DOI: 10.1039/b000000x/

- 1 B. Chen, Y. Yang, F. Zapata, G. Lin, G. Qian, E. B. Lobkovsky, *Adv. Mat.*, 2007, **19**, 1693.
- 2 L. Armelao, S. Quici, F. Barigelletti, G. Accorsi, G. Bottaro, M. Cavazzini, E. Tondello, *Coord. Chem. Rev.*, 2010, **254**, 487.
- 3 Y. Cui, H. Xu, Y. Yue, Z. Guo, J. Yu, Z. Chen, J. Gao, Y. Yang, G. Qian, B. Chen., *J. Am. Chem. Soc.*, 2012, **134**, 3979.
- 4 J. Yu, L. Zhou, H. Zhang, Y. Zheng, H. Li, R. Deng, Z. Peng, Z. Li., *Inorg. Chem.*, 2005, **44**, 1611.
- 5 a) Y. Cui, Y. Yue, G. Qian, B. Chen., *Chem. Rev.*, 2012, **112**, 1126. b) M. D. Allendorf, C. A. Bauer, R. K. Bhakta, R. J. Houk, *Chem. Soc. Rev.*, 2009, **38**, 1330. c) K. Binnemans, *Chem. Rev.*, 2009, **109**, 4283. d) J. C. Bünzli, C. Piguet., *Chem. Soc. Rev.*, 2005, **34**, 1048.
- 6 D. J. Tranchemontagne, Z. Ni, M. O' Keeffe, O. M. Yaghi, *Angew. Chem. Int. Ed.*, 2008, **47**, 5136.
- 7 C. Janiak. *Dalton Trans.*, **2003**, 2781.
- 8 M. Osada, K. Akatsuka, Y. Ebina, H. Funakubo, K. Ono, K. Takada, T. Sasaki, *ACS Nano* 2010, **4**, 5225.
- 9 K. Akatsuka, M. Haga, Y. Ebina, M. Osada, K. Fukuda, T. Sasaki, T., *ACS Nano*, 2009, **3**, 1097.
- 10 J. N. Coleman, M. Lotya, A. O'Neill, S. D. Bergin, P. J. King, U. Khan, K. Young, A. Gaucher, S. De, R. J. Smith, I. V. Shevets, S. K. Arora, G. Stanton, H.-Y. Kim, K. Lee, G. T. Kim, T. Hallam, J. J. Boland, J. J. Wang, J. F. Donegan, J. C. Grunlan, G. Moriarty, A. Shmeliov, R. J. Nicholls, J. M. Perkins, E. M. Grievson, K. Theuwissen, D. W. McComb, P. D. Nellist, V. Nicolosi., *Science*, 2011, **311**, 568.
- 11 J.-C. Tan, P. J. Saines, E. G. Bithell, A. K. Cheetham, *ACS Nano*, 2012, **6/1**, 615.
- 12 a) D. Ghoshal, A. Kumar Ghosh, G. Mostafa, J. Ribas, N. Ray Chaudhuri, *Inorg. Chim. Acta.*, 2007, **360**, 1771. b) N. Guillou, C. Livage, G. Férey, *Eur. J. Inorg. Chem.*, 2006, **24**, 4963. c) N. Guillou, C. Livage, W. Van Beek, M. Noguès, G. Férey, *Angew. Chem. Int. Ed.*, 2003, **42(6)**, 644. d) P. M. Forster, A. K. Cheetham, *Angew. Chem. Int. Ed.*, 2002, **41(3)**, 457. e) R. Vaidyanathan, S. Natarajan, C. N. R. Rao, *Inorg. Chem.*, 2002, **41 (20)**, 5226. f) A. R. Burbank, M. C. O'Sullivan, N. Guillou, C. Livage, G. Férey, N. Stock, A. K. Cheetham, *Solid State Sci.*, 2005, **7(12)**, 1549. g) P. M. Forster, N. Stock, A. K. Cheetham, *Angew. Chem Int. Ed.*, 2005, **44**, 7608. h) P. M. Forster, A. R. Burbank, C. Livage, G. Férey, A. K. Cheetham, *Chem. Commun.*, 2004, **10 (4)**, 368. i) J. Perles, M. Iglesias, C. Ruiz-Valero, N. J. Snejko, *Mater. Chem.*, 2004, **14**, 2683. j) M. C. Bernini, E. V. Brusau, G. E. Narda, G. E. Echeverría, C. G. Pozzi, G. Punte, C. W. Lehmann, *Eur. J. Inorg. Chem.*, 2007, **5**, 684. k) M. C. Bernini, F. Gándara, M. Iglesias, N. Snejko, E. Gutierrez-Puebla, E. V. Brusau, G. E. Narda, M. A. Monge, *Chem. Eur. J.*, 2009, **15 (19)**, 4896. l) C. A. F. de Oliveira, F. F. da Silva, I. Malvestiti, V. Rodrigues dos S. Malta, J. D. L. Dutra, N. B. da Costa Jr., R. O. Freire, S. Alves Jr., *J. Mol. Struct.*, 2013, **1041**, 61.
- 13 a) M. C. Bernini, V. A. de la Peña-O'Shea, M. Iglesias, N. Snejko, E. Gutierrez-Puebla, E. V. Brusau, G. E. Narda, F. Illas, M. A. Monge, *Inorg. Chem.*, 2010, **49**, 5063. b) P. J. Saines, M. Steinmann, J. C. Tan, H. H. M. Yeunga, A. K. Cheetham, *CrystEngComm.*, 2013, **15**, 100. c) G. E. Gomez, M. C. Bernini, E. V. Brusau, G. E. Narda, W. A. Massad, A. Labrador, *Cryst. Growth Des.*, 2013, **13**, 5249.
- 14 J. Zhou, C.Y. Sun, L. P. Jin, *Polyhedron*, 2007, **23**, 4025.
- 15 H. Q. Hao, J. X. Li, L. Li, M. X. Peng, *J. Coord. Chem.*, 2012, **65**, 2561.
- 16 J. C. Bünzli, S. Comby, A. S. Chauvin, C. D. B. Vandevyver, *J. Rare Earth*, 2007, **25**, 257.
- 17 D. T. de Lill, N. S. Gunning, C. L. Cahill, *Inorg. Chem.*, 2005, **44**, 258.
- 18 W. J. Rieter, K. M. L. Taylor, H. An, W. Lin; W. Lin, *J. Am. Chem. Soc.*, 2006, **128**, 9024.
- 19 D. T. de Lill, A. de Bettencourt-Dias, C. L. Cahill, *Inorg. Chem.*, 2007, **46**, 3960.
- 20 P. C. R. Soares-Santos, L. Cunha-Silva, F. A. Almeida Paz, R. A. Sá Ferreira, J. Rocha, T. Trindade, L. D. Carlos, H. I. S. Nogueira, *Cryst. Growth Des.*, 2008, **8**, 2505.
- 21 Y. Sun, J. Zhang, G.-Y. Yang, *Chem. Commun.*, **2006**, 4700.
- 22 J. Jin, S. Niu, Q. Han, Y. Chi, *New J. Chem.*, 2010, **34**, 1176.
- 23 A. Carné, C. Carbonell, I. Imaz, D. MasPOCH, *Chem. Soc. Rev.*, 2011, **40**, 291.
- 24 R. C. Huxford, J. Della Rocca, W. Lin, *Curr. Opin. Chem. Biol.*, 2010, **14**, 262.
- 25 O. Shekhah, J. Liu, R. A. Fischer, Ch. Wöll, *Chem. Soc. Rev.*, 2011, **40**, 1081.
- 26 SHELXTL, version 5.0; Siemens Analytical X-ray Instruments Inc.: Madison, WI, 1995.
- 27 Software for the SMART System V5.04 and SHELXTL V 5.1; Bruker-Siemens Analytical X-ray Instrument, Inc.: Madison, WI, 1998. SHELXTL, version 5.0; Siemens Analytical X-ray Instruments Inc.: Madison, WI, 1995.
- 28 G. M. Sheldrick, *Acta Cryst.*, 2008, **A64**, 112.
- 29 SAINT data collection and procedure software for the SMART system; Siemens Analytical X-ray Instruments, Inc.: Madison, WI, 1995.
- 30 E. Dowty, ATOMS for Windows, a computer program for displaying atomic structure, Version 3.1; Shape Software: Kingsport, TN, 1995.

- 31 Mercury CSD 2.0 - new features for the visualization and investigation of crystal structures, C. F. Macrae, I. J. Bruno, J. A. Chisholm, P. R. Edgington, P. McCabe, E. Pidcock, L. Rodriguez-Monge, R. Taylor, J. van de Streek, P. A. Wood, *J. Appl. Cryst.*, 2008, **41**, 466.
- 32 C. Janiak, *J. Chem. Soc., Dalton Trans.*, **2000**, 3885.
- 33 C. Lee, C. Mellot-Draznieks, B. Slater, W. G. Wu, T. A. Harrison, C. N. R. Rao, A. K. Cheetham, *Chem. Commun.*, **2006**, 2687.
- 34 V.A. Blatov, A.P. Shevchenko, D.M. Proserpio, *Cryst. Growth Des.*, 2014, **14**, 3576.
- 35 a) E. V. Alexandrov, V. A. Blatov, A. V. Kochetkov, D. M. Proserpio, *CrystEngComm.*, 2011, **13**, 3947; b) M. O'Keefe, O. M. Yaghi, *Chem. Rev.*, 2012, **112**, 675.
- 36 V. A. Blatov, M. O'Keefe, D. M. Proserpio, *CrystEngComm.*, 2009, **12**, 44.
- 37 A. Monge, F. Gándara, E. Gutiérrez-Puebla, N. Snejko, *CrystEngComm.*, 2011, **13**, 5031.
- 38 K. Nakamoto, *Infrared and Raman Spectra of Inorganic and Coordination Compounds*, 5th ed., John Wiley & Sons, Inc., USA, 1997, 182.
- 39 M. C. Bernini, J. C. Garro, E. V. Brusau, G. E. Narda, E. L. Varetti, *J. Mol. Struct.*, 2008, **888**, 113.
- 40 (a) M. E. Farago, S. Amirhaeri, *Inorg. Chim. Acta*, 1984, **81**, 205. (b) A. Tapparo, S. Health, P. Jordan, G. Moore, A. Powell, *J. Chem. Soc., Dalton Trans.*, **1996**, 1601. (c) E. V. Brusau; J. C. Pedregosa; G. E. Narda, A. P. Ayala, E. A. Oliveira, *J. Argent. Chem. Soc.*, 2004, **92 (1/3)**, 43.
- 41 A. Bétard, R. A. Fischer, *Chem. Rev.*, 2012, **112**, 1055.
- 42 H. Guo, Y. Zhu, S. Wang, S. Su, L. Zhou, H. Zhang, *Chem. Mater.*, 2012, **24**, 444–450.
- 43 B. Guo, Y. Zhu, S. Qiu, J. A. Lercher, H. Zhang, *Adv. Mater.*, 2010, **22**, 4190–4192.
- 44 P. Horcajada, T. Chalati, C. Serre, B. Gillet, C. Sebrie, T. Baati, J. F. Eubank, D. Heurtaux, P. Clayette, C. Kreuz, J-S. Chang, Y. K. Hwang, V. Marsaud, P-N. Bories, L. Cynober, S. Gil, G. Férey, P. Couvreur, R. Greg, *Nature Mat.*, 2010, **9**, 172.
- 45 O. Shekhah, J. Liu, R-A. Fischer, Ch. Wöll, *Chem. Soc. Rev.*, 2011, **40**, 1081.
- 46 W. J. Rieter, K. M. L. Taylor, H. An, W. Lin, W. Lin, *J. Am. Chem. Soc.*, 2006, **128**, 9024.
- 47 Z. Ni, V. Masel, *J. Am. Chem. Soc.*, 2006, **128**, 12394.
- 48 T. Tsuruoka, S. Furujawa, Y. Takashima, K. Yoshida, S. Isoda, S. Kitagawa, *Angew. Chem. Int. Ed.*, 2009, **48**, 4739.
- 49 A. Beeby, I. M. Clarkson, R. S. Dickins, S. Fauljner, D. Parker, L. Royle, A. S. de Sousa, J. A. G. Williams, M. Woods, *J. Chem. Soc., Perkin Trans.*, 1999, **2**, 493.
- 50 A.-S. Chauvin, F. Gumy, D. Imbert, J.-C. G. Bünzli, *Spectrosc. Lett.*, 2004, **37**, 517.
- 51 A. Huignard, T. Gacoin, J.-P. Boilot, *Chem. Mater.*, 2000, **12**, 1090.
- 52 (a) R. Reisfeld, C. K. Jørgensen, *Lasers and Excited States of Rare Earths*; Springer Verlag: Heidelberg, Germany, 1977. (b) F. X. Gan, *Optical and Spectroscopic Properties of Glass*; Springer Verlag: Berlin, 1992. (c) R. Reisfeld; C. K. Jørgensen, *Struct. Bond.*, Berlin, 1982, **49**, 1.
- 53 A. M. Kaczmarek, K. Van Hecke, R. Van Deun, *Inorg. Chem.* 2014, **53**, 9498
- 54 Y.-L. Gai, F.-L. Jiang, L. Chen, Y. Bu, K.-Z. Su, S. A. Al.Thabaiti, M.-C. Hong, *Inorg. Chem.*, 2013, **52(13)**, 7658.
- 55 Y.-L. Gai, F.-L. Jiang, L. Chen, M. Wu, K.-Z. Su, J. Pan, X. Wan, M.-C. Hong, *Cryst. Growth Des.*, 2014, **14** 1010.

Graphical Abstract

**Highlight**

Three new layered 2D Ln-MOFs based on 2-phenylsuccinate, Sm, Eu and Eu/Gd showed a suitable platform for obtaining exfoliatable frameworks with promising photoluminescent properties for potential applications as thin films.